JGR Oceans

RESEARCH ARTICLE
10.1029/2019JC015510

Special Section:
Contributions from the Physics of Estuaries and Coastal Seas meeting, 2018

# A Conceptual Model of a River Plume in the Surf Zone

S. E. Kastner[1,2], A. R. Horner-Devine[1], and J. M. Thomson[1,2]

[1]Department of Civil & Environmental Engineering, University of Washington, Seattle, WA, USA, [2]Applied Physics Lab, University of Washington, Seattle, WA, USA

**Abstract** We use observations from the Quinault River, a small river that flows into an energetic surf zone on the West Coast of Washington state, to investigate the interaction between river and wave forcing. By synthesizing data from moorings, drifters, and Unmanned Aerial System video, we develop a conceptual model of this interaction based on three length scales: the surf zone width, $L_{SZ}$; the near-field plume length, $L_{NF}$; and the cross-shore extent of the channel, $L_C$. The relationships between these length scales show how tidal variability and bathymetric effects change the balance of wave and river momentum. The most frequently observed state is $L_{SZ} > L_{NF}$. Under these conditions the surf zone traps the outflowing river plume and the river water's initial propagation into the surf zone is set by $L_{NF}$. When the river velocity is highest during low water, and when wave forcing is low, $L_{NF} > L_{SZ}$ and river water escapes the surf zone. At high water during low wave forcing, $L_C > L_{SZ}$, such that minimal wave breaking occurs in the channel and river water escapes onto the shelf. Based on the discharge, wave, and tidal conditions, the conceptual model is used to predict the fate of river water from the Quinault over a year, showing that approximately 70% of the river discharge is trapped in the surf zone upon exiting the river mouth.

**Plain Language Summary** Small rivers are an important source of sediment, nutrients, and pollutants to the coastal ocean, but they are less well studied than their larger siblings. The coastal discharge from small rivers often meets large breaking waves in the surf zone. Our work investigates the effect of the large waves present at the mouth of one such river, the Quinault River in Washington State. We find that the fate of Quinault River water is determined by the relative importance of river, wave, and depth effects, all of which are modulated by the tide. When wave forcing dominates, river water is trapped in the surf zone. When river forcing dominates, river water escapes the surf zone. The difference in depth between the offshore channel and the rest of the beach can also allow river water to escape the surf zone by reducing the effect of the wave forcing. When we apply our conceptual model to 1 year of wave, river, and tide data, we predict that 70% of Quinault River discharge is trapped in the surf zone. The sediment and pollutants carried by this trapped river water can thus have important impacts on beach erosion, public health, and local ecology.

**Key Points:**
- A conceptual model using three length scales describes the behavior of the Quinault River plume
- When wave forcing dominates over river forcing, freshwater is trapped in the surf zone
- Tidal variability allows river water to escape due to river momentum and bathymetric effects

**Correspondence to:**
S. E Kastner,
skastner@uw.edu

**Citation:**
Kastner, S. E., Horner-Devine, A. R., & Thomson, J. M. (2019). A conceptual model of a river plume in the surf zone. *Journal of Geophysical Research: Oceans*, *124*, 8060–8078. https://doi.org/10.1029/2019JC015510

Received 25 JUL 2019
Accepted 16 OCT 2019
Accepted article online 31 OCT 2019
Published online 19 NOV 2019

## 1. Introduction

Small freshwater discharges represent an important source of sediment, nutrients, and pollutants to the coastal ocean. Relative to their discharge, such rivers export proportionally more sediment to the coastal ocean, as they often lack deltas that sequester sediment (Milliman & Syvitski, 1992). The net effect of the export of sediment, nutrients, and pollutants from small rivers can be especially large in the midlatitudes, where small rivers comprise a large fraction of total river discharge to the coastal ocean (Izett & Fennel, 2018).

Most studies of coastal plumes have focused on large river sytems, and our understanding of small river plumes is poor (Garvine, 1977; Horner-Devine et al., 2015; Kilcher et al., 2012; MacDonald & Geyer, 2004). The interaction of plume dynamics with surf zone processes is a key component in the dynamics of small river discharges. Recent studies have shown that the relative importance of river plume momentum and alongshore or cross-shore surf zone dynamics can determine the fate of river water that flows into the surf zone (Rodriguez et al., 2018; Wong et al., 2013).

Small river mouths are often unengineered, allowing surf zone wave breaking to occur near or at such outflows. In regions with higher population densities, engineered structures such as jetties are present at most river mouths, preventing wave breaking and the influence of surf zone dynamics on buoyancy and

momentum-driven river plume processes (Clark et al., 2010; Hally-Rosendahl et al., 2014; Horner-Devine et al., 2015).

### 1.1. Surf Zone Processes

Wave breaking is the dominant driver of physical processes in the surf zone, where waves break near the shore as a result of depth limitation. Depth-limited breaking occurs at a critical value of $\gamma = \frac{H_S}{d}$, where $H_S$ is the significant wave height and $d$ is depth (Miche, 1944). Theoretical work finds that for a solitary wave, $\gamma = 0.781$, while observational studies have found that random waves have a range $0.3 < \gamma < 0.6$ (Janssen & Battjes, 2007; Miche, 1944; Raubenheimer et al., 1996). Breaking waves lose radiation stress (i.e., the momentum flux associated with the waves), and the resulting momentum drives nearshore currents and coastal setup (Longuet-Higgins, 1970; Longuet-Higgins & Stewart, 1961, 1962). Breaking waves are also a significant source of turbulence near the ocean surface, especially in the surf zone, where near-surface values of dissipation rate reach $\epsilon \approx 10^{-2}$ m$^2$/s$^3$ (Feddersen, 2012; Feddersen & Trowbridge, 2005; Thomson, 2012; Thornton & Guza, 1986).

Transport of freshwater from a river entering the surf zone could be reasonably expected to be influenced by surf zone circulation processes, as has been shown for passive tracers (Brown et al., 2015; Clark et al., 2010; Hally-Rosendahl et al., 2014). The strongest surf zone circulation is driven in the alongshore direction by obliquely directed breaking waves (Feddersen et al., 1998; Longuet-Higgins, 1970). The cross-shore circulation, relevant for exchange between the surf zone and the inner shelf, is generally weak (Clark et al., 2010; Hally-Rosendahl et al., 2014; MacMahan et al., 2004; Reniers et al., 2009). Exceptions are rip currents, which can generate significant exchange between the surf zone and the inner shelf (Clark et al., 2010; Haller et al., 2002; Hally-Rosendahl & Feddersen, 2016; Kumar & Feddersen, 2017). Other cross-shore mechanisms for transport are Stokes drift (onshore lagrangian motion) and undertow (offshore return flow) (Fewings et al., 2008; Stokes, 1847). Wave-driven alongshore currents are therefore a likely transport mechanism for surf zone freshwater, with cross-shore flow being of secondary importance (excepting rip currents).

### 1.2. River Plume Processes

Coastal river discharges are a significant driver of cross-shelf transport of freshwater and river-borne material, which has motivated significant efforts to understand and model their dynamics. In the near-field of river plumes, the dynamics are governed by the outflow momentum and buoyancy (Hetland, 2010; Horner-Devine et al., 2015; Garvine & Monk, 1974; O'Donnell, 1990) and are typically described using the upper layer Froude number, $Fr_1 = \frac{u}{\sqrt{g' h_p}}$. Here $u$ is the upper layer velocity, $g' = \frac{g\Delta\rho}{\rho_0}$ is the reduced gravity associated with the plume stratification, $\Delta\rho$, and $h_p$ is the plume layer depth. The plume near-field is considered to be the region where momentum effects dominate over buoyancy effects and so the upper layer is supercritical ($Fr_1 > 1$) (Garvine, 1977; Hetland, 2010; Horner-Devine et al., 2015). Eventually, mixing causes the upper layer Froude number to drop and the near-field ends where $Fr_1 = 1$ (Hetland, 2010; Luketina & Imberger, 1987; McCabe et al., 2008). Beyond this point, plume dynamics are strongly influenced by buoyancy and are characterized in terms of the gravity current speed, $u_{gc} = \sqrt{g' h_p}$, as well as local wind forcing and earth′s rotation.

Mixing influences the upper layer Froude number through the entrainment of high-density, low-momentum ambient water due to shear-driven turbulence. Mixing is characterized as a density flux through the base of the plume $\rho_e w_e$, where $\rho_e$ is the entrained density and $w_e$ is the entrainment velocity (MacDonald & Geyer, 2004; McCabe et al., 2008; Hetland, 2010). Plume entrainment is often parameterized in terms of the local bulk Richardson number, $Ri_b$ (Christodoulou, 1986; Ellison & Turner, 1959; Yuan & Horner-Devine, 2013). This relationship varies over different regimes of $Ri_b$, but the normalized entrainment velocity $\delta = w_e/u$ is generally dependent on $Ri_b$. The inflow bulk Richardson number, $Ri_{b0} = \frac{g_0' h_0}{u_0^2}$, best characterizes this functionality such that $\delta = aRi_{b0}^{-1/2}$, where $a \approx 0.02$ and the subscript 0 indicates that the bulk Richardson number is evaluated at the river mouth (Christodoulou, 1986; Yuan & Horner-Devine, 2013). Calculations of normalized entrainment vary between $3 \times 10^{-3} < \delta < 6 \times 10^{-2}$, with field studies (MacDonald & Geyer, 2004) reporting lower values than laboratory studies (Ellison & Turner, 1959; Yuan & Horner-Devine, 2013). Field observations of turbulent kinetic energy dissipation associated with plume entrainment vary between $10^{-5} < \epsilon < 10^{-3}$ W/kg (Jurisa et al., 2016; Kilcher et al., 2012; MacDonald & Geyer, 2004).

### 1.3. Wave-Plume Processes

Most previous studies of the interactions of river plume and wave dynamics have focused on large river plumes. The results of numerical model studies show that turbulence due to wave breaking increases mixing in the far-field surface plume layer (Gerbi et al., 2013, 2015). Elevated mixing has also been observed at the offshore front of the Columbia River plume, where strong, sheared currents lead to wave blocking and breaking due to steepness limitation. The turbulence resulting from this wave breaking is scaled by a gradient in wave energy flux across the front and could be downwelled to the base of the plume layer by frontal convergence (Thomson et al., 2014; Zippel & Thomson, 2017). In the near field of large river plumes, wave effects are less clear. Stokes drift causes modest advection (hundreds of meters) of the Columbia river plume (Akan et al., 2017). Large plume depths relative to wave heights in the Fraser River plume shield the plume from mixing due to breaking wave-driven turbulence (Kastner et al., 2018).

At New River Inlet, NC, an unengineered tidal inlet, depth-limited wave breaking is enhanced by the presence of an opposing tidal current, causing waves to steepen and break (Zippel & Thomson, 2015). Preferential breaking can occur on either side of the inlet mouth, away from the deeper channel, forcing a rip current-like circulation that enhances offshore tidal velocities out of the inlet (Olabarrieta et al., 2014).

Rodriguez et al. (2018) show that for an idealized small river entering a surf zone, the percentage of freshwater that remains in the surf zone is related to the ratio of river momentum flux to wave momentum flux. When wave momentum flux dominates, freshwater remains in the surf zone and mixes minimally. When river momentum flux dominates, most freshwater escapes the surf zone and exhibits normal river plume behavior on the shelf, with some freshwater remaining trapped in the surf zone. Wong et al. (2013) show that surf zone trapping of dye released in the mouth of a small creek emptying into the surf zone is determined by the degree to which the creek outflow is turned by wave-driven forcing. When the outflow is significantly turned by wave-driven currents, it is trapped in the surf zone, while a straighter outflow can result in river water reaching the inner shelf. This finding is analogous to that of Rodriguez et al. (2018) in that alongshore wave-driven currents are stronger (for a constant wave angle) when wave forcing is stronger. Rodriguez et al. (2018) and Wong et al. (2013) thus show that wave forcing can trap a small river plume in the surf zone by controlling the cross-shore momentum flux balance or by turning the plume with strong alongshore currents.

### 1.4. Conceptual Model Framework

In this work we propose that the dynamics of a river plume in the surf zone can be understood in terms of the relative magnitudes of three length scales that characterize the governing processes in this interaction: the surf zone width, $L_{SZ}$; the near-field plume length, $L_{NF}$; and the channel length, $L_C$.

The surf zone width, $L_{SZ}$, is a function of the offshore significant wave height, local bathymetry, and the local critical value of $\gamma$. $L_{SZ}$ represents the cross-shore distance over which wave breaking occurs, causing a radiation stress gradient.

Hetland (2010) defines the near-field plume length, $L_{NF}$, based on the plume momentum $M = u_0 Q$, buoyancy $B = g' Q$, and nondimensional entrainment $\delta$, where $u_0$ is the river mouth velocity, $Q$ is the river discharge, and $g'$ is a measure of the density difference between the river mouth and the ambient offshore water. The resulting scaling from Hetland (2010) is

$$L_{NF} = \frac{u_0^{3/2} Q^{1/4}}{g'^{1/2} w_e^{3/4}}. \quad (1)$$

This is a modification of the jet-to-plume length scale, which predicts the region in which the momentum of a jet, rather than its buoyancy, controls the flow (Fischer et al., 1979; Jirka et al., 1981; Jones et al., 2007). With the inclusion of the parameter $\delta$, Hetland (2010) shows that $L_{NF}$ as defined by equation (1) agrees well with the location where $Fr_1 = 1$. A critical assumption for the use of $L_{NF}$ is that the plume is in steady state. In a tidally variable system, this assumption is valid providing that the time scale characterizing the near field, $T_{NF}$, is short compared with tidal time scales. This is evaluated in section 2.3.2.

The channel length, $L_C$, is the cross-shore location where the channel formed by the seaward extension of the river channel into the nearshore bathymetry is no longer deeper than the surrounding bathymetry. At a natural river mouth, sediment transport processes determine this length scale. At an engineered river mouth, the length scale is set by dredging and/or the presence of jetties. We expect that the fate of river

**Table 1**
*The Conditions and River Water Behaviors Associated With Each Conceptual Mode*

| Mode | Condition | Predicted behavior |
|---|---|---|
| Wave dominance | $L_{SZ} > L_{NF}$ and $L_{SZ} > L_C$ | River water exits the river mouth and is trapped in the surf zone by wave forcing |
| River dominance | $L_{NF} > L_{SZ}$ | River water exits the surf zone as its momentum overcomes breaking wave forcing |
| Bathymetric dominance | $L_C > L_{SZ}$ | River water exits the river mouth and reaches the inner shelf largely bypassing wave forcing due to minimal wave breaking in the channel |

water will be predicted by the relative magnitude of these scales as they vary over the course of a tidal cycle. When the wave forcing is sufficiently energetic relative to the strength of the river discharge, the surf zone will be wider than the near-field plume length ($L_{SZ} > L_{NF}$). In this case we anticipate that the plume loses momentum before exiting the surf zone and freshwater is trapped. If the opposite is true, the discharge penetrates through the surf zone to the inner shelf. As we will show in section 3.3.3, we observe a third mode of behavior that completes the conceptual picture. When the surf zone is narrower than the channel length ($L_{SZ} < L_C$) freshwater escapes by bypassing the wave forcing. These three modes of behavior form the conceptual model that we will test and apply in interpreting our data. They are summarized in Table 1.

## 2. Methods

### 2.1. Observational Setup

We made observations at the Quinault River, in Taholah, WA, between 24 April and 5 May 2017. During the study period, the tidal range measured by the USGS Point Grenville gage varied from 1.5 to 3 m (Figure 2a). The discharge at the river mouth is calculated as 1.5× the USGS measured discharge at Quinault Lake per local knowledge from the Quinault Nation Division of Natural Resources and falls from ~220 to ~110 $m^3/s$ during the study period (Figure 2b). The tidally reconstructed velocity at the surface in the river mouth (see section 2.2) varies from ~0.5 to 2 m/s (Figure 2c). The wave height observed by the AWAC varied from ~1 to 2 m, with a mean wave angle of ~ $6.5 \pm 6.2°$ relative to shore normal (Figure 2d). Offshore winds from NDBC 46041 varied from 5 to 10 m/s, mostly from the northwest and southeast (Figure 2e).

Our observational program consisted of three main components: Drifter deployments from inside the river inlet, nearshore and inlet-based moorings, and unmanned aerial system (UAS) flights from the shore.

#### 2.1.1. Drifter Deployments

We deployed two types of SWIFT drifters from inside the river mouth throughout each day of the study, SWIFT v3 and SWIFT v4 (Thomson, 2012; Thomson et al., 2019). All of these SWIFTs measure wave properties using either an Inertial Measurement Unit (v3, v4) or a Global Positioning System (v3). SWIFT v4 and

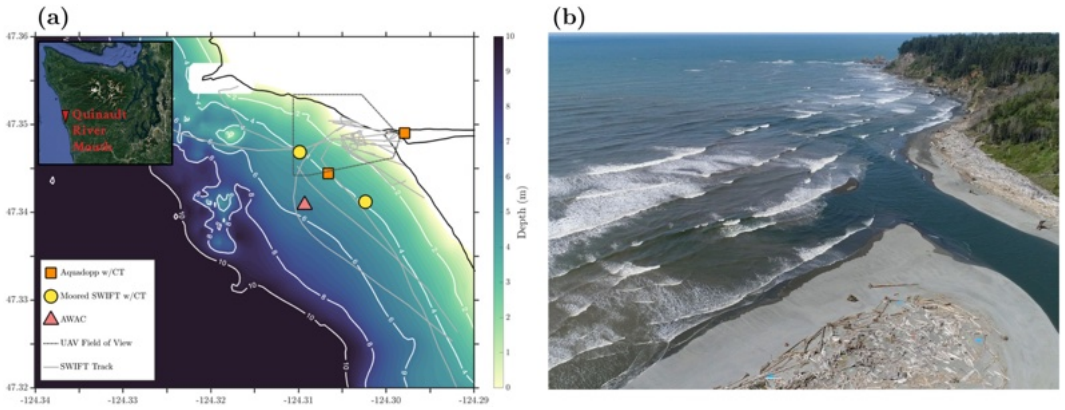


**Figure 1.** The observational field campaign at the Quinault River mouth. Panel (a) shows a map of deployed instruments and bathymetry. Color indicates depth, and isobaths are given as white lines with notations in meters. Orange squares indicate moorings using Nortek Aquadopp ADCPs, yellow circles indicate moorings using SWIFTs, and the red triangle indicates the offshore AWAC. The UAS field of view is given as a dashed-dotted black line, and SWIFT drift tracks are solid gray lines. The inset Google Earth image shows the location of the Quinault river mouth on the Washington coast. Panel (b) is an example UAS perspective image from 28 April 2017, when $H_S = 1.5$ m, $Q = 171$ $m^3/s$, and $\eta = 1.3$ m.

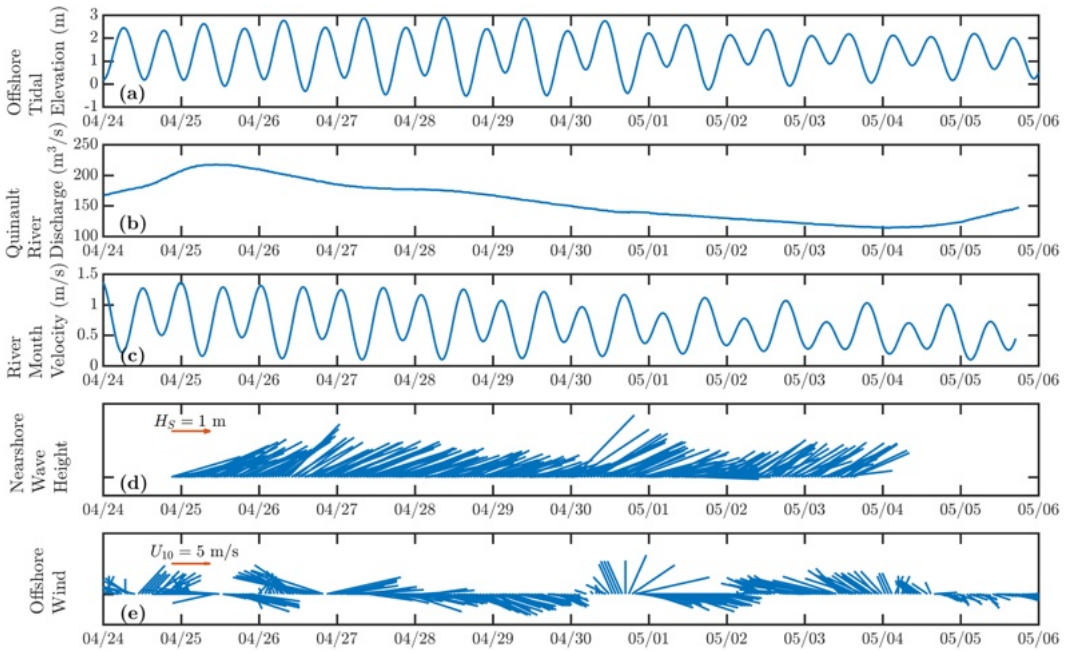


**Figure 2.** Time series of the observational period of (a) the tidal elevation at Point Grenville, (b) the modified discharge from the Lake Quinault USGS gage, (c) the tidally interpolated river mouth velocity, (d) the AWAC wave height and direction (east to the right), and (e) the offshore wind speed and direction from NDBC 46041 (same convention as wave direction).

SWIFT v3 measure salinity and temperature using an Aanderaa 4319 CT sensor. SWIFT v3 measures either near-surface turbulence using an uplooking Nortek Aquadopp HR or a velocity profile using a downlooking Nortek Aquadopp. SWIFT v4 measures both near-surface turbulence and a velocity profile using a downlooking Nortek Signature 1000 (HR). The Signature 1000 is also used to measure water depth. The SWIFT v3 has a draft of 1.2 m, the SWIFT v4 has a draft of 0.25 m, and the $\mu$SWIFT has a draft of 0.5 m. SWIFT v3 and v4 sample in 512-s bursts every 12 min, such that there are five bursts each hour, starting on the 0-, 12-, 24-, 36-, and 48-min marks.

The drifters were deployed from a small boat station at the center of the river channel close to the river mouth mooring (Figure 1). We conducted a total of 60 drifter deployments during daylight hours throughout the study period, spanning all tidal phases, a variety of tidal amplitudes, a variety of incident wave conditions, and a twofold variation in river discharge (Figure 2). Drifters were deployed in staggered pairs with one released 3 min before the start of a given data collection burst and one released at the start of a given data collection burst. This deployment scheme maximized observations in the surf zone within the constraints of the 12-min burst sampling scheme.

In order to qualitatively assess tidal influence on the system, we define three categories of drifter behavior: (1) escaping the surf zone, (2) nearly escaping the surf zone, or (3) remaining trapped in the surf zone (Table 2). Drifters that escape the surf zone transit to the inner shelf, where their trajectories are determined by the local inner shelf circulation. Drifters that nearly escape the surf zone follow river momentum nearly to the surf zone edge before losing offshore momentum, turning around to travel onshore, and beaching near the river mouth. Trapped drifters lose their offshore momentum before reaching the edge of the surf zone and beach quickly after deployment.

**Table 2**
*Distribution of SWIFT Deployments by Behavior and Type of Drifter*

| Drifter type | Escape | Near-escape | Trap | Total |
|---|---|---|---|---|
| SWIFT v3 | 4 | 6 | 18 | 28 |
| SWIFT v4 | 4 | 4 | 9 | 17 |
| Total | 8 | 10 | 27 | 45 |

### 2.1.2. Moorings

We deployed five moorings: three nearshore moorings positioned at the outer edge of the surf zone in 4-m water depth, a Sea Spider tripod with a Nortek Acoustic Waves and Currents (AWAC) instrument in 6-m water depth and a Datawell DWR-G4 buoy (telemetry wave parameters only, raw data not recorded) in 15-m water depth with an Onset HOBO temperature sensor at 0.5 m and a HOBO pressure/temperature (PT) sensor at 1.5 m. The offshore

(WaveRider and Sea Spider) moorings were deployed on 24 April, while the nearshore moorings were deployed on 28 April, when wave conditions were lower. The three nearshore moorings all included two YSI 600LS CTD sensors at 1 and 3 m below the surface, HOBO temperature sensors at 1.5, 2, and 2.5 m, and HOBO PT sensors at 4 m below the surface. The middle mooring had a PT sensor at 2 m instead of a temperature sensor. Each nearshore mooring also included a surface following downlooking acoustic Doppler current profiler. On the north and south moorings, this was a SWIFT v4 with an integrated Nortek Signature 1000, while the middle mooring had a Nortek Aquadopp mounted on a Doppcat floatation system. All of these moorings were recovered on 3 May. The nearshore moorings were deployed progressively closer to shore southward in the array roughly following the 4-m isobath, the north mooring was ~900 m offshore, the middle mooring was ~750 m offshore, and the south mooring was ~550 m offshore (Figure 1).

The moorings in the river inlet included a HOBO PT sensor at the dock to measure the tidal signature in the inlet, as well as a Nortek Aquadopp mounted on a Doppcat small instrumented catamaran that was deployed in the river mouth while a team was onsite during daylight hours. This Doppcat had a HOBO PT sensor attached to its anchor. The PT sensor at the dock was deployed starting 26 April and ending 5 May. These deployments captured three quarters of a neap-spring cycle.

#### 2.1.3. UAS Operations

We conducted UAS flights using a DJI Phantom 4 Pro equipped with a 4k video camera near the river mouth, imaging from an altitude of approximtely 120 m. These flights lasted ~10 min each, including ascent and descent. We flew the UAS during daylight hours, normally concurrent with a SWIFT deployment, in order to capture video of the SWIFTs traversing the surf zone near the river mouth. We placed 5–8 ground control points on the bar near the river mouth in order to rectify the UAS video (Holman et al., 2017). Twenty-eight flights were made during the study period.

### 2.2. Momentum Flux Calculations

#### 2.2.1. River Momentum Flux

We calculate the river momentum flux, $u^2h$, where the velocity $u$ is the surface river velocity immediately inside the river mouth measured with the Doppcat ADCP, and $h$ is the river channel depth. The channel depth $h$ is determined by combining measurements of depth from the ADCP and the dock pressure sensor. The dock depth was consistently shallower than the river mouth by 1.5 m (not shown), and so we use the more complete dock tide gage time series, adjusted by this factor, in our calculations. In order to fill in the gaps in both time series, we use the *UTide* Matlab functions (Codiga, 2011). In this time series reconstruction, we consider the M2, S2, and K1 tidal constituents while allowing a trend over time to account for the decrease in discharge during the study period. We perform this time series reconstruction on both the river mouth ADCP and dock tide gage in order to be consistent in our calculations. This time series reconstruction does not allow for the constant river velocity and depth observed during maximum flow at low water. These effects will partially cancel, as the velocities have maxima higher than the observed constant while the depths have minima lower than the observed constant. This will likely cause overestimates of peak river momentum flux.

#### 2.2.2. Wave Radiation Stress

We calculate the cross-shore component of the shoreward wave radiation stress as

$$S_{xx} = g \int_{f0}^{\infty} E(f) \left( \frac{c_g(f)}{c_p(f)} (\cos^2\theta(f) + 1) - \frac{1}{2} \right) \mathrm{d}f, \tag{2}$$

where $E(f)$ is the spectral wave energy in $m^2$/Hz, $c_g(f)$ is the wave group velocity associated with a frequency at the water depth where the measurement is made, $c_p(f)$ is the wave phase speed associated with a frequency at the water depth where the measurement is made, and $\theta(f)$ is the wave direction from shore normal associated with a frequency. This formulation assumes that the waves are shore normal, which is approximate, but not exact, at the AWAC (where this calculation is made). We ignore the role of wave direction in the calculation of $S_{xx}$; thus, the calculation represents the maximum cross-hore radiation stress for a given wave energy flux and depth.

### 2.3. Length and Velocity Scale Calculations

#### 2.3.1. Surf Zone Width

We use the AWAC measurements of local wave conditions, the UAS images, and the SWIFT v4 water depth measurement to estimate surf zone width. The SWIFT v4 water depth measurement is used to generate a depth profile for the beach south of the Quinault River mouth. This calculation uses detided SWIFT depth

measurements averaged on a 30-m cross-shore grid. We use the same gridding to obtain channel bathymetry. The average depths are then smoothed using a low-pass Butterworth filter. To resolve near-shore bathymetry, we extract the waterline from 25 georectified time-averaged UAS images at varying tidal stages. By combining the waterline extractions with the SWIFT South beach bathymetry and smoothing again, we obtain a cross-shore bathymetry profile. We calculate surf zone widths using this bathymetry profile, the AWAC measurements, the wave shoaling equations and assuming a critical $\gamma = H_S/d$, where $H_S$ is significant wave height and $d$ is water depth. We calculate the increase in wave height to the point of breaking using a shoaling constant $K_S$, such that $H = K_S H_o$ and $K_S = \sqrt{\frac{c_{go}}{c_{gb}}}$, where $H$ is a shoaled wave height, $H_o$ is the wave height at the AWAC, $c_{go}$ is the group velocity at the AWAC, and $c_{gb}$ is the group velocity at the onset of wave breaking. We assume that waves break in shallow water, and so $c_{gb} = \sqrt{g d_b}$. By assuming $\gamma_b = 0.6$, we can thus calculate the depth at breaking such that $d_b = \left(\frac{H_o}{\gamma_b}\frac{c_{go}^{1/2}}{g^{1/4}}\right)^{4/5}$. We choose $\gamma_b = 0.6$ to match the conditions when no breaking is seen in the channel in the UAS imagery (Figures 3a–3d). We then look up the corresponding cross-shore distance of $d_b$ at the tidal stage associated with that time and calculate a surf zone width $L_{SZ}$ by measuring the distance to the breakpoint from the origin of our coordinate system, the maximum onshore position of the river mouth. This length scale includes the tidal modulation of the waterline in the nominal surf zone width for ease of comparison. Examples of the surf zone width calculation can be seen in Figure 4 for both the channel and the South beach bathymetry.

This methodology does not take into account wave-current interaction in and near the offshore channel. Such interactions cause refraction, steepening, and breaking in surface waves and could be expected to influence the surf zone width (Kirby & Chen, 1989; Zippel & Thomson, 2015, 2017). We neglect such interactions in our calculation of surf zone width due to their spatially complex nature. Discussion of the potential effects of wave-current interaction can be found in section 4.4. In general, we expect depth-limited breaking to be a much more important process in this system.

#### 2.3.2. Near-Field Plume Length

We calculate, $L_{NF}$, the offshore extent of the plume nearfield, based on equation (1). Here $M = M_0 = u_0 Q_0$, $B = B_0 = g' Q_0$, and $\delta = w_e/u_0$. We take $u_0$ to be the tidally varying river mouth velocity from the UTide reconstructed ADCP surface velocity (2.2) and $Q_0 = u_0 b_0 h_0$ to be the river discharge. The effective channel width, $b_0$, is determined according to $b_0 = \frac{\int Q \mathrm{d}t}{\int u_0 h_0 \mathrm{d}t}$, where $Q$ is the modified USGS Quinault Lake gage discharge. The reduced gravity for the system, $g'$, is calculated using the average ambient water density at the nearshore moorings such that $\Delta\rho = 24$ kg/m$^3$. The entrainment velocity $w_e$ is calculated from the inflow bulk Richardson number using the methodology from Yuan and Horner-Devine (2013) such that $\delta = 0.03 Ri_{b0}^{-1/2}$. To calculate $Ri_{b0} = \frac{g' h_0}{u_0^2}$, we use the river mouth velocity and depth, along with the reduced gravity for the system. The median result from this calculation yields $w_e = 8$ mm/s. This is similar to results from the Fraser liftoff zone, where $1 < w_e < 7$ mm/s (MacDonald & Geyer, 2004). In order to minimize noise, we use the tidally phase-averaged quantity $\overline{L_{NF}}$ to define the modes of the conceptual model. The surf zone width is not similarly averaged so as not to eliminate the surf zone width's dependence on wave conditions during a given bin of tidal phase. Using the surf zone width concurrent with each drifter deployment on both axes introduces autocorrelation but allows a more complete dynamical understanding of the conceptual modes.

As discussed in section 1.4, $L_{NF}$ is used in this analysis as a representation of the scale of the near-field plume at one point in time, even though it is based on variables that vary significantly over the course of a tidal cycle. This characterization is only meaningful if the timescale over which $L_{NF}$ adjusts is short relative to the tidal period. We estimate the near-field adjustment timescale as $T_{NF} = L_{NF}/u_0$, which is approximately 10 min for the Quinault. This is much less than one quarter of a tidal cycle, indicating that $L_{NF}$ is able to adjust to tidal changes in the forcing variables. In larger plume systems, $T_{NF}$ is expected to be longer and more caution must be taken in applying this scaling. For example, at the Columbia River, $u = 2.5$ m/s, $Q = 7{,}000$ m$^3$/s, and $w_e = 2$ mm/s (McCabe et al., 2008), resulting in $L_{NF} \sim 8.5$ km and $T_{NF} = 1$ hr.

## 3. Results

### 3.1. Tidal Variability of River and Wave Forcing

Drifter behavior, as defined in section 2.1.1, shows a clear dependence on tidal phase (Figure 5a); all drifter escapes and near escapes occur at high or low water. This result suggests that tidally varying depth and

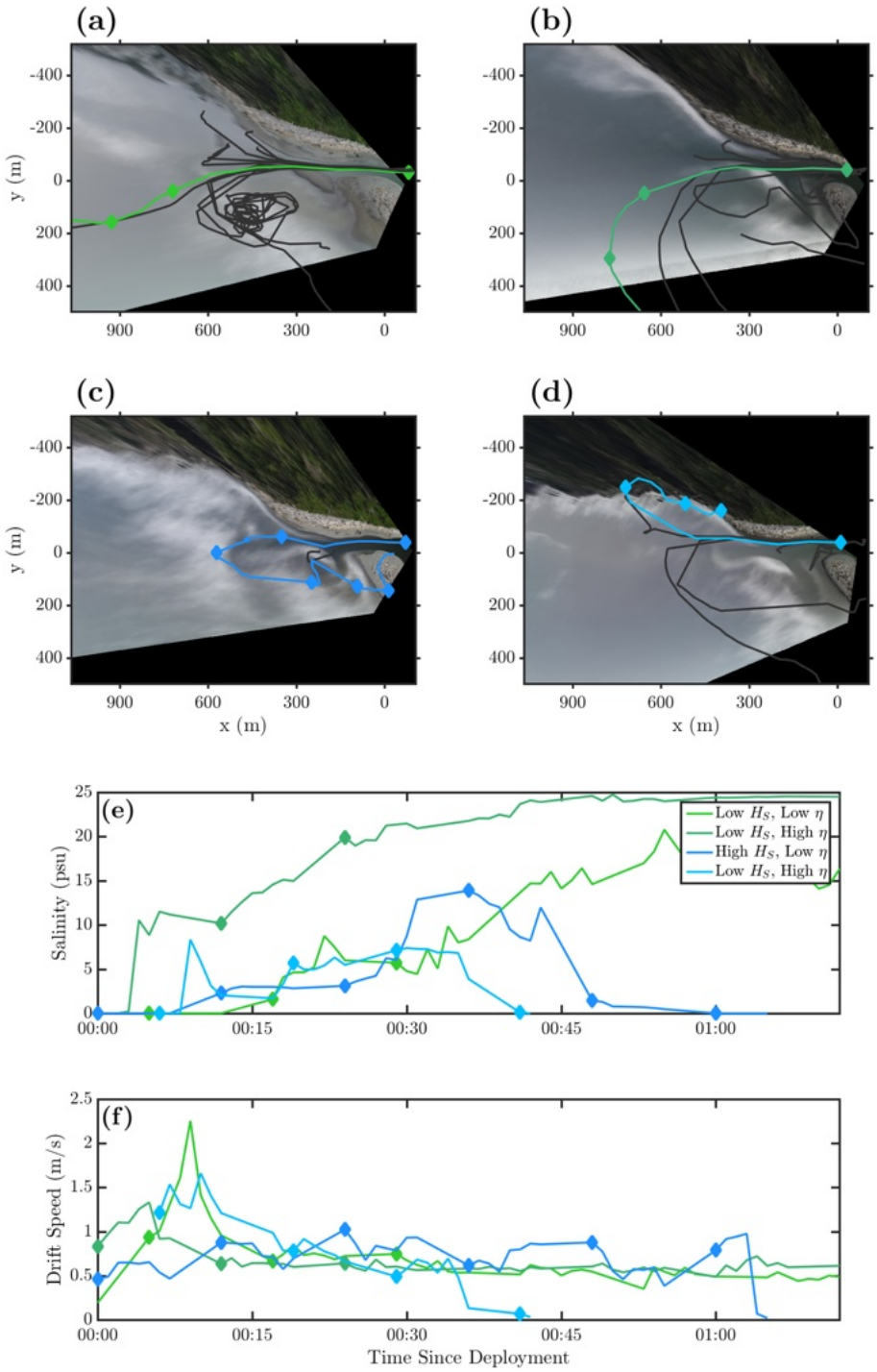


**Figure 3.** Example UAS images, drifter tracks, and drifter data time series for varying wave and tidal conditions. Images have been rectified and averaged over 10 min. Panel (a) shows low water and low wave forcing, (b) shows high water and low wave forcing, (c) shows low water and high wave forcing, and (d) shows high water and high wave forcing. Panels (e) and (f) show time series plots of near-surface salinity and drift speed, respectively, for the same colored drift tracks in panels (a)–(d). Filled diamonds occur indicate the corresponding point in space on (a)–(d) to a point in time in (e) and (f).

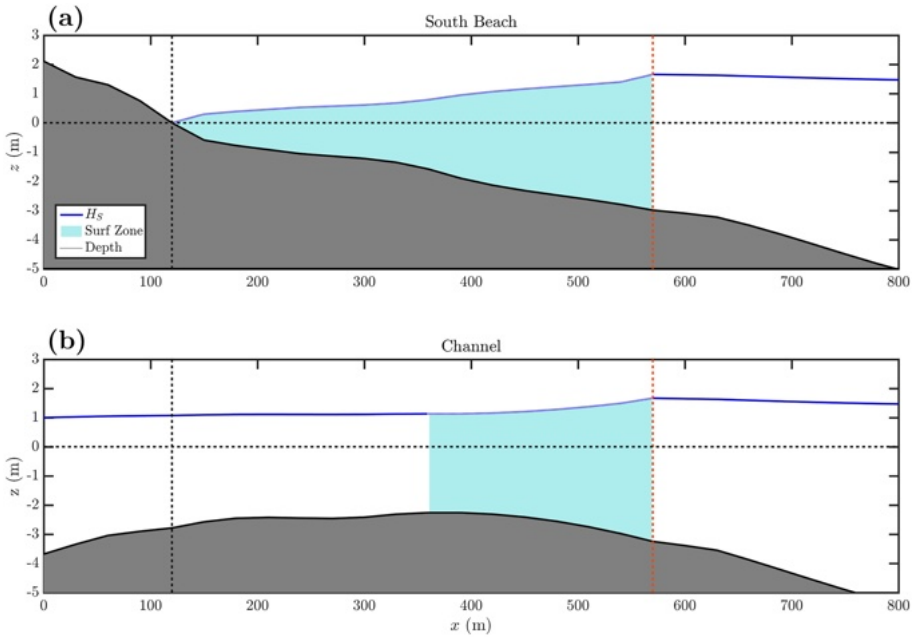


**Figure 4.** Wave shoaling over cross-shore bathymetric profiles on the (a) South beach and (b) channel at $\eta = 1.05$ m. The shaded gray region indicates the bathymetric profile. The solid blue line indicates a cross-shore position where a wave of height $H_S$ would not be expected to break via depth limitation, while the dotted blue line and corresponding shaded area indicate a region of expected wave breaking. The horizontal dashed black line indicates the still water level at $\eta = 1.05$ m, and the vertical dashed black line indicates the cross-shore location at which $d = 0$ m on the South beach. The red dashed line indicates the predicted break point.

discharge velocity strongly influence the fate of river water in the surf zone. The maximum velocity at the river mouth occurs just before low water, and minimum velocity occurs just after high water. Drifter behavior is thus related to tidal variations in the momentum flux, $u^2h$, in the Quinault system (Figures 5c and 5d); escapes occur only near maxima of tidal stage or river velocity. The incident wave radiation stress does not vary tidally. Thus, low water drifter escapes are coincident with a tidal maximum in river momentum flux relative to a tidally constant wave momentum flux. Escapes also occur at high water, when river momentum is at its lowest. Observations from drifters that escape the surf zone indicate an increase in near-surface salinity as the drifters transit onto the inner shelf. This increase occurs more quickly for high water escapes than low water escapes (Figure 3e). Trapped drifters tend to measure freshwater while remaining in the surf zone (Figure 3e). These behaviors will be further examined in section 3.3.

Time series of salinity measurements show episodic occurrences of freshwater at the nearshore moorings (Figure 6b) that can be compared with the variability of river momentum flux and wave radiation stress (Figure 6d) over the 5 days when all the moorings were concurrently deployed. The lowest salinities during freshwater events were observed furthest from the river mouth in alongshore position at the south mooring. These salinities reach as low as 13.7 psu during the strongest event at the south mooring and between 20 and 25 psu during other events. These salinities differ from ambient water by 15 psu during the strongest event and by 3–5 psu during other events (Figure 6b). The freshwater events occur when river momentum is near its maximum at low water and thus when the ratio $\frac{u^2h}{S_{xx}}$ is near a local peak. This correlation is not necessarily indicative of river water reaching the shelf due to its own momentum; however, the salinity minima are usually observed closest to shore at the south mooring, which is sometimes inside the surf zone. Therefore, observations of freshwater at nearshore moorings are concurrent with maximum river momentum at low water but are not necessarily indicative of freshwater escaping the surf zone, as the surf zone width is also at maximum at low water and could be larger than the near-field plume length. This observation suggests that the surf zone width is an important scale in this system and motivates the conceptual model proposed in section 1.4.

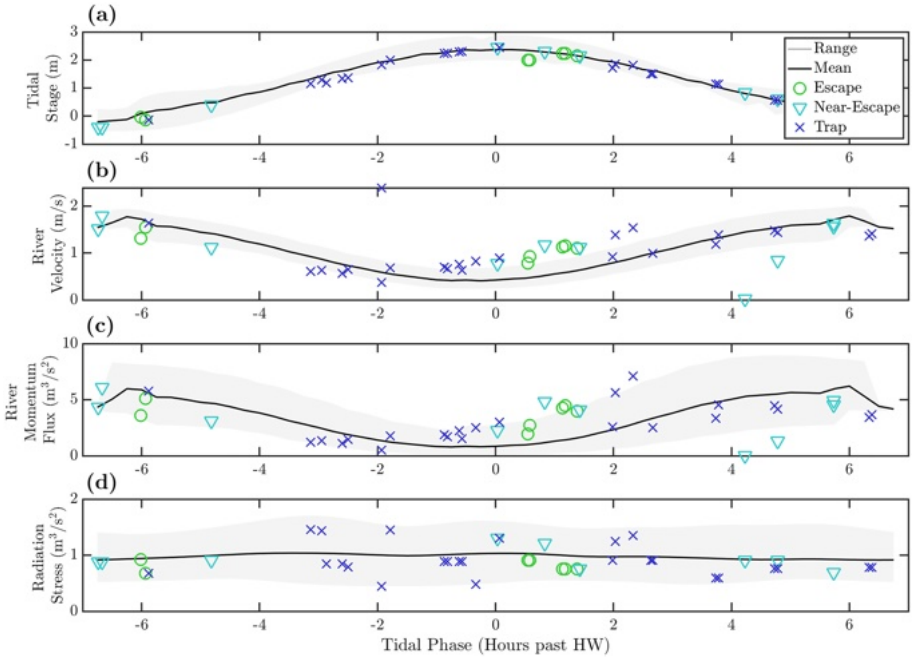


**Figure 5.** Tidally phase-averaged measured quantities and calculations using moorings or gage data (solid black lines), and drifter data (markers). Markers indicate drifter behavior: green circles are escapes, teal triangles are near escapes, and blue crosses are traps. The gray shaded area indicates the range of values for a measurement or calculation at a given tidal phase. Panel (a) shows tidal stage from the Point Grenville gage, (b) shows river velocity from the inlet mooring or measured by a drifter deployment, (c) river momentum flux from the inlet mooring or a drifter deployment, and (d) radiation stress from the AWAC.

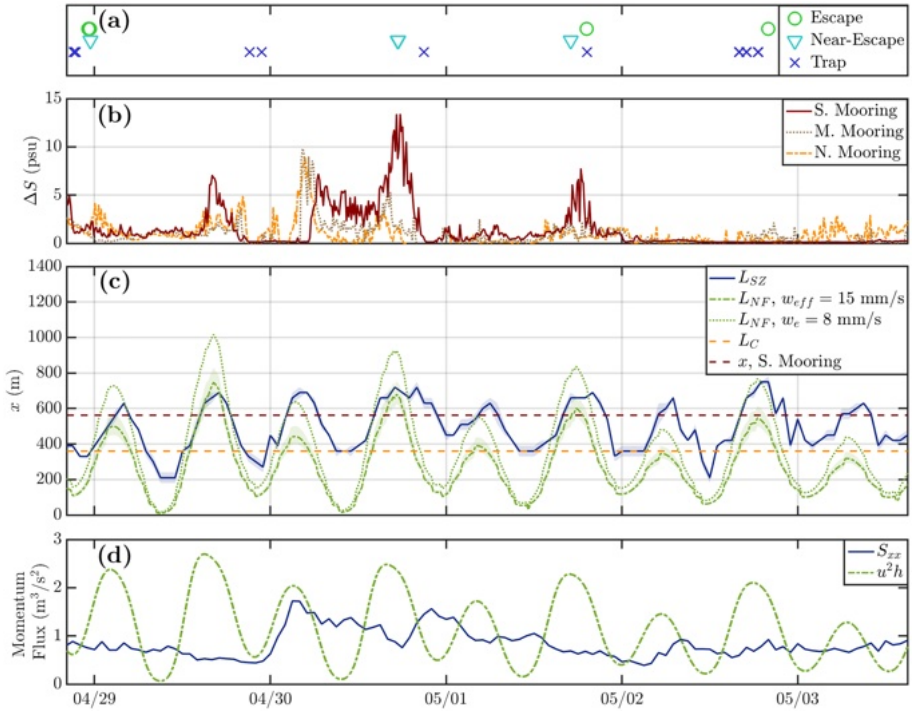


**Figure 6.** Time series of (a) drifter behavior, with the same symbols as in Figure 5; (b) time series of salinity difference from 3 to 1 m at the south (red solid line), middle (brown dashed line), and north (orange dashed-dotted line) nearshore moorings; (c) time series of surf zone width (blue), near-field length (green), and channel length (orange). The near-field length is calculated with $w_e = 8$ mm/s (green dashed line) and a range of $12 < w_{eff} < 18$ mm/s (purple shaded region) with $w_{eff} = 15mm/s$ as the dashed-dotted green line. The dashed burgundy line indicates the cross-shore position of the south mooring; (d) time series of wave radiation stress, $S_{xx}$ at the AWAC and river momentum flux, $u^2h$ at the inlet mooring.

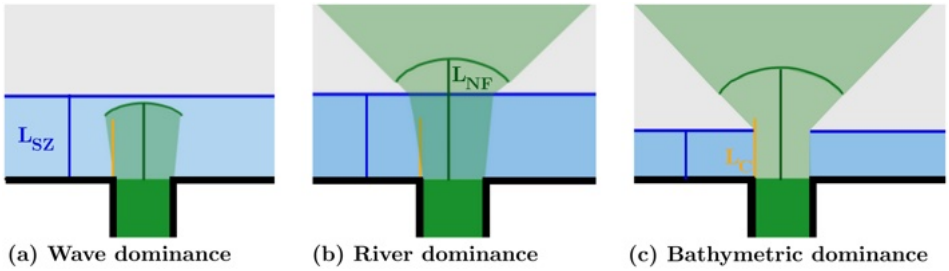


**Figure 7.** Schematics of each mode of the conceptual model, with the surf zone width indicated by the blue line, the near-field length by the green line, and the channel length by the orange line. Panel (a) shows wave dominance, (b) shows river dominance, and (c) shows bathymetric dominance. The dominant length scale for each mode is labeled.

### 3.2. Length Scale Comparison and Drifter Fate

The length scales $L_{NF}$ and $L_{SZ}$ also vary tidally. The near-field length and the river momentum flux have similar dependencies, and so it follows that $L_{NF}$ is also at maximum at low water and minimum at high water (Figure 6c). The surf zone width as defined in section 2.3.1 varies tidally as the shoreline moves toward or away from a fixed reference point and as such is at maximum at low water and a minimum at high water. Therefore, $L_{NF}$ and $L_{SZ}$ vary in phase with each other over the course of a tidal cycle. The tidal variability of the near-field length is larger than that of the surf zone width, and so the quantity $L_{NF}/L_{SZ}$ is maximum at low water and minimum at high water.

In Figure 8, every SWIFT v3 and v4 drift concurrent with the AWAC deployment is plotted in terms of its cross-shore excursion normalized by surf zone width, $x_{max}/L_{SZ}$, and the ratio $\overline{L_{NF}}/L_{SZ}$. Drifters may be quantitatively defined as having escaped the surf zone when $x_{max}/L_{SZ} > 1$ and as trapped in the surf zone when $x_{max}/L_{SZ} < 1$. Most drifters are observed to be trapped in the surf zone but escapes do occur when $\overline{L_{NF}}/L_{SZ}$ is low or high, coincident with high or low water, respectively. The surf zone width is low for high water escapes, potentially indicating bathymetric dominance, while the near-field length is large for low water escapes, potentially indicating river dominance.

Trapping events occur when wave forcing dominates over river forcing and channel bathymetry does not play a significant role in determining the breakpoint. During times when the moorings are not in the surf zone, the salinity is generally high and stratification is generally low, corroborating this observation (Figure 6b). Closer to shore, drifter observations indicate the presence of trapped freshwater. The wave dominated behavior may thus be associated with a cross-shore density gradient through the surf zone. Trapped drifters are typically associated with $\gamma > 0.6$ at the edge of the channel, indicating that waves have broken or are breaking in the channel during these drifter deployments. The maximum drifter excursions during wave dominated conditions are smaller than the surf zone width (Figure 8a). Escapes can occur when river forcing dominates over wave forcing at low water or bypasses wave forcing when there is minimal wave breaking in the channel. Drifters that escaped the surf zone were subject to the forcing present on the inner shelf; all but two such drifters beached within hours or days of deployment after traveling along the coast. When river forcing is large at low water, high stratification (low surface salinity) is sometimes observed at the moorings, while high water escapes are generally associated with low offshore stratification (Figure 6b). These observations are corroborated by drifter measurements of salinity, which show a faster increase in salinity for a drifter escape at high water than a drifter escape at low water (Figure 3e). When drifters escape the river mouth at high water, waves are not breaking at the offshore edge of the channel ($\gamma < 0.6$). Low water drifter escapes often occur near the daily maximum in $L_{NF}$ and river momentum flux $u^2h$.

The behaviors described above can be classified into wave, river, or bathymetric dominant modes by the conceptual model.

### 3.3. Conceptual Model

#### 3.3.1. Wave Dominant Conditions

The most common behavior observed in our study is that wave breaking traps river water in the surf zone. Based on the definition of the near field, the plume has lost most of its initial momentum once it reaches

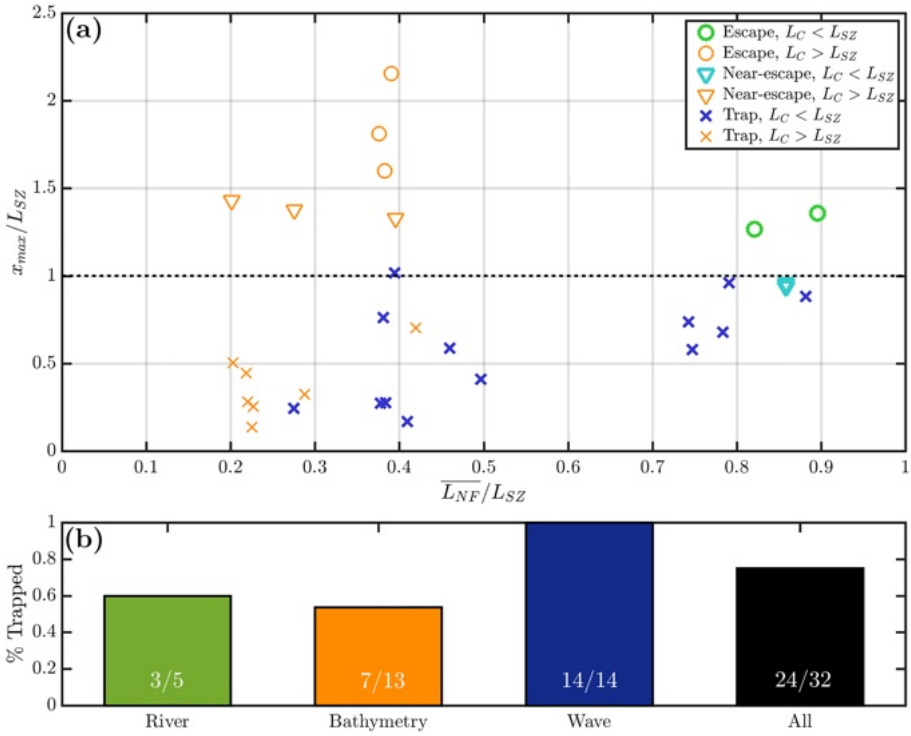


**Figure 8.** Panel (a) shows drifter excursion normalized by surf zone width plotted against the tidally phase averaged near-field length normalized by surf zone width. Marker symbol indicates drifter behavior as in Figure 5, and orange marker color indicates drifts during bathymetric dominated conditions. Panel (b) shows the percent of drifters trapped during each mode of behavior and all drifts. The 32 drifts shown here were v3 or v4 SWIFTs deployed concurrently with the AWAC.

$L_{NF}$. If it is still in the surf zone at that point, the wave forcing appears to block further seaward movement (Figure 7a).

Wave dominant conditions can be defined for the length scales presented in Figure 8 as when $\overline{L_{NF}} > mL_{SZ}$ and $nL_{SZ} < L_C$. Here, $m$ and $n$ are constants close to unity and $L_C \approx 360$ m (section 3.3.3). In our observations, $m = 0.8$ and $n = 0.83$. Thus, once a drifter approaches the edge of the surf zone, there exists the possibility of an escape while $\overline{L_{NF}} > 0.8L_{SZ}$. Likewise, when the surf zone width narrows such that $0.83L_{SZ} < L_C$, there exists the possibility of a bathymetric dominated escape. The value $m = 0.8$ is chosen such that drifts where $x_{max}/L_{SZ} > 1$ when $L_{NF}/L_{SZ}$ is high (low water) are classified as river dominated escapes. Similar logic leads us to define $n = 1.2$, such that drifts where $x_{max}/L_{SZ} > 1$ and $L_{NF}/L_{SZ}$ is low (high water) are classified as bathymetric dominated escapes. This classification results in 100% of drifts during wave dominant conditions being trapped in the surf zone. The difference of $m$ and $n$ from unity is partially due to unresolved short time scale variability in forcing, such as the timing of a drifter release relative to the timing of the maximum wave height in a wave group. Specifically for $n$, measurement error in SWIFT bathymetry estimates could play a role in $n$ being less than unity. Additionally, it is likely that $m$ & $n$ do not define exact thresholds between the conceptual modes, that is, the value of $m$ could represent a value of $\overline{L_{NF}}/L_{SZ}$ where river dominated escapes occur more frequently. Similar logic could be applied to the value of $n$ for the bathymetric and wave dominant modes. More drifts would be needed to fully develop a more probabilistic approach to the conceptual model.

The observed trapping of river water in the surf zone is consistent with the modeling results of Rodriguez et al. (2018), who find that the percentage of freshwater within the surf zone scales with increased wave forcing. An important distinction of this result, however, is the dependence of $L_{NF}$ on $w_e$, indicating that mixing, as well as momentum, can be important in determining wave effects. This is discussed in more detail in section 4.1.

#### 3.3.2. River Dominant Conditions

Calculations of $\overline{L_{NF}}$ and $L_{SZ}$ show that $\overline{L_{NF}} > mL_{SZ}$ at low water, such that river dominant conditions, can occur when the river momentum is at its daily maximum (Figure 7b). There are two cases where drifters escape the surf zone when $\overline{L_{NF}}$ and river momentum flux are at their maximum at low water, such that $\overline{L_{NF}} > mL_{SZ}$ and $u^2h > S_{xx}$ (Figure 8). Therefore, 60% of deployed drifters are trapped in the surf zone when river dominant conditions occur (Figure 8b). As some, but not all, drifters escape the surf zone during river dominant conditions, $\overline{L_{NF}} > mL_{SZ}$ is a necessary but not sufficient condition for river water escape.

Rodriguez et al. (2018) conclude that higher river momentum can result in a larger percentage of freshwater transport onto the inner shelf. Their numerical model simulations do not include tides, but we suggest here that the conditions in their higher river momentum and wave forcing simulations are analogous to those leading to maximum values of $L_{NF}$ and $L_{SZ}$ that we observe at low water at the Quinault. The most similar simulation to Quinault conditions uses a discharge $Q = 100$ m$^3$/s and a wave height $H_S = 1$ m, which results in 10% of river water being trapped in the surf zone. During the two instances of river water escapes at low water we observed with drifter deployments, $Q \approx 140$ m$^3$/s and $H_S \approx 1.4$ m.

#### 3.3.3. Bathymetric (Channel) Dominant Conditions

For low wave conditions at high water, $nL_{SZ} < L_C$, indicating that wave breaking is initiated onshore of the end of the offshore channel (thus, there is minimal breaking in the channel). In order for wave forcing to trap river water in the surf zone, wave-driven momentum must dominate over river momentum. Wave-driven momentum in the surf zone is caused by the spatial gradient in the cross-shore component of the shoreward radiation stress, and this gradient is directly related to wave breaking. When (and where) wave breaking does not occur, there is minimal opposition to the river momentum and river water can escape from the surf zone (Figure 7c). This can occur in the the natural offshore channel, which is analogous to the dredged channels often constructed in engineered river mouths. For the Quinault, the channel diverges from the beach bathymetry profile at a cross-shore distance $L_C \approx 360$ m and is on average 1 m deeper than the beach bathymetry before dropping to a maximum depth of 4.5 m inside the river inlet. Thus, breaking will only occur in the channel for $nL_{SZ} > L_C$, when $\gamma > 0.6$ inside the channel. Bathymetric dominance is indicated in Figure 8a by orange symbols. Immediately after high water, all drifts reach $x_{max}/L_{SZ} > 1$ until $nL_{SZ} > L_C$, around 2 hr after high water (not shown). Interestingly, while $nL_{SZ} < L_C$ before high water, drifts result in traps at values close to $L_{NF}$, despite $\gamma < 0.6$ at the channel edge during most such drifts.

When bathymetric dominant conditions occur, 55% of drifters are trapped in the surf zone (Figure 8b). As with river dominant conditions, this implies that bathymetric dominance is necessary but not sufficient for the escape of river water. Our results suggest a minimum river momentum that is required for these escapes to occur, specifically the value observed just as the river momentum increases following high water. This minimum river momentum is equal to the minimum wave momentum in the channel, which occurs when $\gamma < 0.6$. The wave momentum is nonzero due to the breaking of some waves that are larger than $H_S$ (i.e., the breaking criterion is statistical, and the one third of waves larger than $H_S$ may break even when $\gamma$ is subcritical). Before high water, the river momentum falls below this threshold, but as the river momentum increases after high water, escapes can occur.

Breaking occurs on either side of the channel when $nL_{SZ} < L_C$ and may increase outflow currents and thus the probability of escape during bathymetric dominant conditions. The alongshore gradients of radiation stress introduced when breaking occurs near the edges of the channel are similar to bathymetrically driven rip currents. Olabarrieta et al. (2014) show that such a spatial pattern of breaking around a tidal channel introduces a rip-like circulation in the channel, increasing the outflow velocity.

Bathymetric dominance is a significant mechanism for transporting fresh river water onto the inner shelf in the Quinault River system but may not be important in systems with small or zero tides (Rodriguez et al., 2018) because variation in the offshore extent of the surf zone is lower. Other systems with a deep channel offshore of the river mouth and a steep beach at high water may also export river water to the shelf in this manner.

Rodriguez et al. (2018) find that the percentage of freshwater trapped in the surf zone scales with the ratio of river momentum flux. This gives similar results to the scaling of $L_{NF}$ versus $L_{SZ}$ presented in the present work. The tidal variability we examine in this paper is similar to the variable parameter space explored in the numerical studies of Rodriguez et al. (2018), with three notable distinctions. First, the minima and maxima of $L_{NF}$ and $L_{SZ}$ are colocated within the tidal cycle at high water and low water, leading to coupled dynamics.

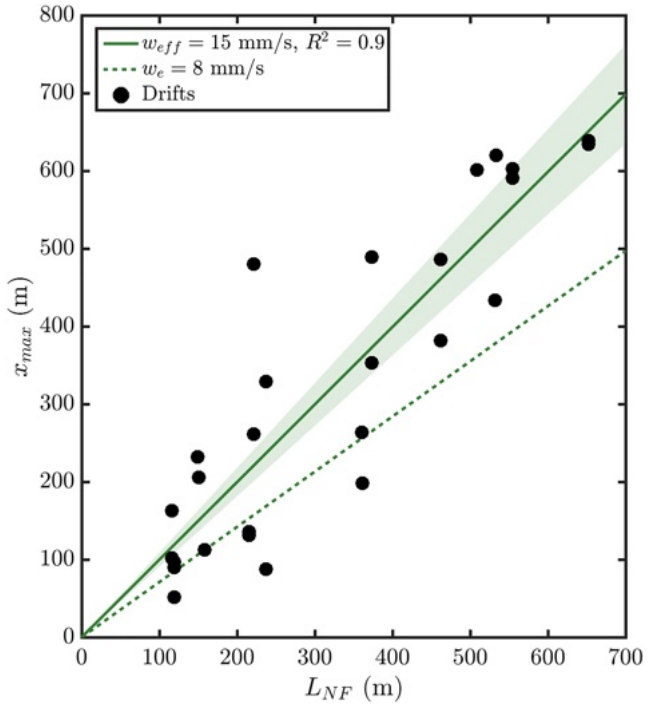


**Figure 9.** The relationship between near-field length and drifter excursion. Two fits are shown, one calculated with $w_e = 8$ mm/s (dashed green line) and one calculated with $w_{eff} = 15$ mm/s (solid green line). The shaded area indicates the 95% confidence interval of the slope for the case where $w_{eff} = 15$ mm/s.

Second, the local bathymetry plays a significant role in the transport of river water onto the shelf; when the breakpoint moves onshore of the channel edge, minimal wave breaking-induced momentum is present to counteract the river momentum. Third, the tidal modulation of $L_{NF}$ sets the initial excursion of river water into the surf zone in wave dominated conditions (section 4.1), and it is possible that $L_{NF}$ is modified by breaking wave-induced mixing or momentum.

## 4. Discussion

### 4.1. Scaling Drifter Excursion

We find that the near-field plume length is an important factor in determining the extent to which river water penetrates the surf zone. The maximum drifter excursion for trapped drifters ($x_{max} < L_{SZ}$) varies tidally (Figure 8). In Figure 9, $x_{max}$ is plotted versus the tidally phase averaged near-field plume length $L_{NF}$ for all trapped drifters. We observe a linear trend in this relationship with an $R^2$ value of 0.9. This result suggests that, during trapping conditions, the distance freshwater penetrates into the surf zone is set by $L_{NF}$. Thus, the tidal variability in the observed excursion distance is largely explained by the variability in $L_{NF}$ associated with the tidal fluctuations in velocity and depth at the river mouth.

There are several possible sources of variability in the relationship between $x_{max}$ and $L_{NF}$. We expect, however, that entrainment resulting from wave breaking turbulence in the surf zone will be a dominant source of variability; it will significantly increase $w_e$ above the value predicted for shear mixing in the absence of waves and decrease $L_{NF}$. In this section we investigate the relationship between $x_{max}$ and $L_{NF}$, defining an effective entrainment velocity, $w_{eff}$, which accounts for the enhanced turbulence associated with wave breaking. The value of $w_{eff} = 15$ mm/s is based on the fit in Figure 9, assuming that all the variability can be accounted for by entrainment. This is clearly a simplification of a very complex system but provides useful estimates for understanding the possible mixing enhancement in the surf zone. The predicted value of $w_e = 8$ mm/ based on Yuan and Horner-Devine (2013) and Christodoulou (1986) underpredicts the drifter excursion (Figure 9). Since $w_{eff} > w_e$, we conclude that a higher effective entrainment better characterizes the relationship between $L_{NF}$ and $x_{max}$. Calculations of $L_{NF}$ made using $w_e = 8$ mm/s yield larger values, which in turn increase the value of $m$ such that $m \approx 1.2$ for a lower entrainment velocity. This increase of $m$ above unity is physically unintuitive and statistically unlikely. We expect that river water will escape the surf zone when $L_{NF} > L_{SZ}$ ($m = 1$) because once river water is outside of the surf zone its propagation is no longer opposed by the landward force from breaking waves. This indicates that $w_e = 8$ mm/s is too low to properly represent the observed dynamics. The effective increase of entrainment in the presence of breaking waves could indicate that the high levels of turbulence in the surf zone lead to more plume mixing.

The relationship evident in Figure 9 suggests that drifters stop when they reach $L_{NF}$, which corresponds to the point where the initial river momentum falls below the buoyant gravity current speed. Thus, this result implies that the buoyant gravity current speed is less than the opposing cross-shore wave velocities in the surf zone. The latter can be estimated based on Stokes' drift (Stokes, 1847). Based on estimates from our mooring measurements, the average Stokes' drift and gravity current velocities are 0.13 and 0.08 m/s, respectively. Thus, Stokes' drift is generally larger than the gravity current speed. The plume may therefore be stopped from propagating offshore as a buoyant gravity current in the surf zone.

The mixing and entrainment rate due to wave breaking in the surf zone is an active area of research, with no canonical estimate available to compare to plume entrainment rates. However, the turbulent kinetic energy dissipation rate that would be associated with wave-driven mixing in the surf zone is generally higher than the dissipation rate associated with shear-driven mixing in a river plume. Near-surface dissipation rates in the surf zone can reach order $\epsilon = 10^{-2}$ W/kg (Feddersen & Trowbridge, 2005), while plume dissipation rates have been found to be of order $\epsilon = 10^{-4}$ W/kg in medium-sized rivers like the Quinault, such as the Merrimack River in Massachusetts (MacDonald et al., 2013). There are other factors that could contribute

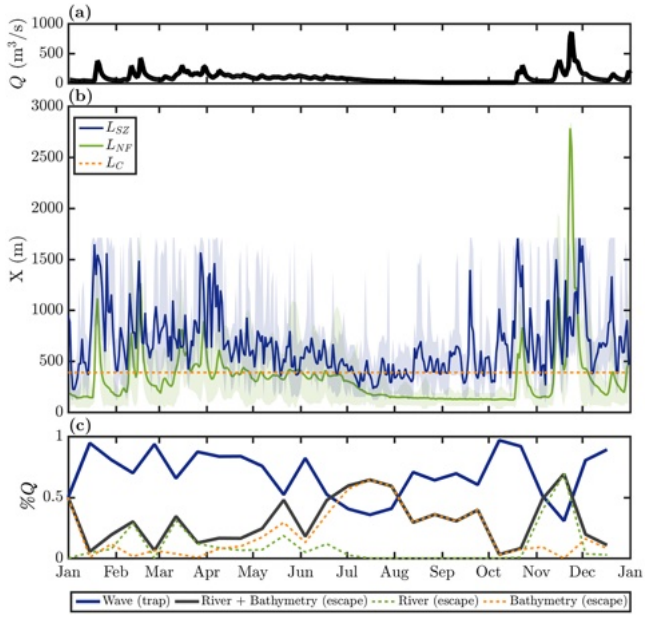


**Figure 10.** The conceptual model, applied to wave, discharge, and tidal amplitude data for the year 2017. Panel (a) shows a time series of discharge; panel (b) shows a time series of the conceptual model length scales averaged over one day, with the maximum and minimum of $L_{SZ}$ and $L_{NF}$ given by the shaded region; and panel (c) shows the percent of river discharge over 14 days governed by each conceptual mode, with the bathymetric and river dominated conditions summed to give a total percent of time when escapes might be expected.

to the drifter excursion differing from the near-field length. For example, wave momentum influences the system dynamics (Rodriguez et al., 2018) and is not included in the near-field length scale. Wave momentum influence would result in a decrease in $w_{eff}$ to compensate for a decrease in total offshore momentum. As $w_{eff}$ is larger than $w_e$, wave mixing is likely the relevant controlling process in the Quinault system. In larger systems it has been suggested that the ratio $H_S/h_p$ determines the extent to which wave-driven turbulence can affect plume mixing (Kastner et al., 2018). SWIFT drifters with three CT sensors that escape the surf zone measure strong stratification in the upper 1.2 m, indicating that $H_S/h_p$ could be in a range where wave-driven turbulence could affect plume mixing.

The drifter excursion for trapped drifters is a reference point for where those drifters stop following the near-surface velocity and begin to be influenced by breaking waves. Thus, the overprediction of $x_{max}$ by $L_{NF}$ for $w_e = 8$ mm/s could also be due to the drifters no longer behaving in a Lagrangian manner onshore of $L_{NF}$. This would suggest that the drifters are no longer Lagrangian once they reach a fraction of $L_{NF}$ determined for $w_e = 8$ mm/s. From the best fit line for $w_e = 8$ mm/s from Figure 9, this excursion would be $x_{max} \approx 0.7L_{NF}$. If non-Lagrangian bias was the most significant driver of $x_{max}$, we would expect the drifter hull type to play a role in drifter fate. This is not the case, however, as the different hull shapes of drifters used in the study do not have an effect on drifter statistics: about one third of each type of SWIFT escape or nearly escape the surf zone (Table 2). It is impossible to completely rule out non-Lagrangian bias in $x_{max}$, but it seems likely that wave-driven mixing and entrainment plays a significant role. Thus, when $L_{NF} < L_{SZ}$ and $L_{SZ} > L_C$, the near-field plume length scale sets that the distance river water can penetrate through the surf zone.

### 4.2. Seasonal Variability of the Fate of Freshwater

In this section we apply the conceptual model developed above to a time series of wave, discharge, and tidal amplitude data from the entire year 2017 in order to assess longer time scale processes. These time series are acquired from the CDIP 036 Grays Harbor buoy, the USGS Quinault Lake stream gage, and the NOAA Pt. Grenville tide gage. All quantities necessary for the calculation of $L_{NF}$, $L_{SZ}$, and $L_C$ can be calculated or used directly from this data, except for $u$ and $h$ at the river mouth. We estimate the water depth at the river mouth as $h = f_h(\eta, Q)$, where $\eta$ is the offshore tidal amplitude and $f_h$ is a multiple linear regression. The river mouth velocity can then be estimated as $u = f_u(h, \partial h/\partial t, Q)$, where $f_u$ is a multiple linear regression. We define the functions $f_h$ and $f_u$ using data collected during our measurement periods. Lower and upper limits are set on the variability of $u$ by enforcing continuity, such that if the estimated volumetric flux out of the river mouth is greater than twice the gage discharge or less than one quarter the gage discharge, the velocity is instead set by the discharge, assuming a channel width of $b = 60$ m. These thresholds are determined by the tidal variability of the river mouth volumetric flow rate observed during the study period. The surf zone width is calculated using the methods from section 2.3.1, assuming that wave conditions along the coast do not vary significantly between Gray's Harbor and the Quinault River mouth and that the bathymetry measurement shown in Figure 4 is representative of the entire year. In general, the length scales calculated from our measurement period and extrapolations from the gage and buoy time series for the same period agree well, with $R^2 = 0.93$ and $R^2 = 0.7$ for $L_{NF}$ and $L_{SZ}$, respectively. The lower correlation in surf zone width is likely caused by spatial heterogeneity in the wave field.

The results of this year-long extrapolation are shown in Figure 10. The length scales vary on seasonal and shorter time scales, driving changes in the fate of the river discharge. In general, $L_{NF}$ varies with $Q$, $L_{SZ}$ varies with $H_S$ (not shown), and both vary with the tide (Figure 10b). The minimum and maximum values of $L_{NF}$ and $L_{SZ}$ shown by the shaded region in Figure 10b are likely to occur for both length scales at high and low water, respectively, and are thus comparable. For simplicity, we assume that river water discharged during bathymetric and river dominated conditions initially escapes the surf zone, and river water discharged during wave dominated conditions is initially trapped in the surf zone. Fourteen-day averaged

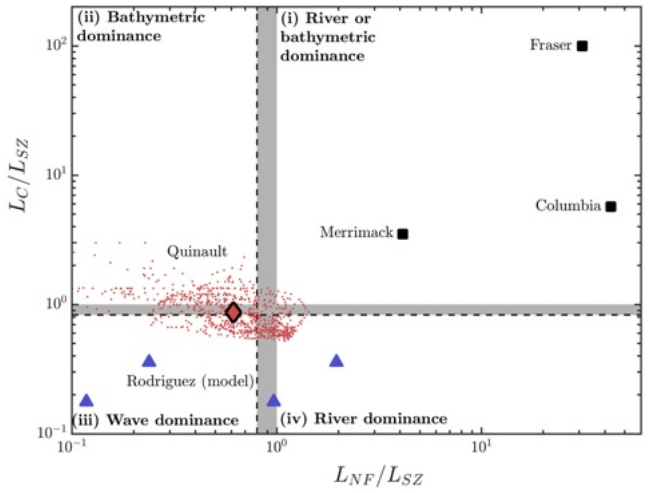


**Figure 11.** River dominance versus wave dominance ($L_{NF}/L_{SZ}$) and bathymetric dominance versus wave dominance ($L_C/L_{SZ}$) for different systems. Data from the Quinault are presented as small red points, with the median value represented as the black lined red diamond. Four different model runs from Rodriguez et al. (2018) with varying $Q$ and $H_S$ are represented as blue triangles. Literature values for the Fraser, Columbia, and Merrimack are represented as black squares. Dashed lines indicate the values of $m$ (vertical) and $n$ (horizontal) reported in section 3.3.1. The gray shaded areas indicate the region between $m$ or $n$ and unity. Four different quadrants are identified using the roman numeral notation defined in section 4.3.

values of the frequency of each mode and the percent of discharge during each are shown in Figure 10c. We can thus use the frequency of occurrence for each mode and the measured discharge to calculate the percent of river water that initially escapes the surf zone or is initially trapped in the surf over the course of one year (Figures 10c and 10d). We find that ~70% of the discharge is trapped in the surf zone, with ~20% escaping due to river dominance and the remaining ~10% escaping due to bathymetric dominance.

Our results suggest that wave dominant conditions are prevalent during most of the year, except during summer and late fall (Figure 10c). As a result, 70% of all river water is trapped in the surf zone immediately after it is discharged from the mouth. During the summer, the model predicts that more than 50% of river water is exported through the surf zone to the inner shelf because wave forcing is low and the bathymetric condition is the dominant mode. Local residents report that the Quinault estuary can be quite salty during these low flow periods in the summer, so the freshwater flux associated with bathymetric escapes in the summer may be low. In late fall, discharge reaches its largest peak of the year during a stormy period and the model predicts more than 50% export of freshwater due to river dominated conditions. The smaller storm-driven peaks in discharge between January and April also result in export driven by river dominance. River dominant export during late fall, winter, and early spring accounts for most of the escaped river water over the course of the year. Not all storms force river water escapes—storms also result in large waves and surf zone widths that can trap river water.

The strong dependence of the conceptual model on tidal variability indicates that the neap-spring cycle should be an important driver of the fate of freshwater, with more energetic spring tides leading to more bathymetric and river dominated escapes than neap tides. The neap-spring signal is only visible in $L_{NF}$ during the summer, when no river dominant conditions are observed. For the rest of the year neap-spring effects are obscured by variability in river discharge and wave height.

### 4.3. Comparison to Other River Systems

The conceptual model developed above can be applied to other rivers by plotting $L_C/L_{SZ}$ against $L_{NF}/L_{SZ}$, using characteristic values of the length scales for other systems (Figure 11). High values of $L_{NF}/L_{SZ}$ indicate river dominance, while low values indicate wave dominance. High values of $L_C/L_{SZ}$ indicate bathymetric dominance, while low values indicate wave dominance. Low values of both ratios are required for wave dominant conditions. Figure 11 may thus be divided into four different quadrants: (i) river or bathymetric dominance, (ii) bathymetric dominance, (iii) wave dominance, and (iv) river dominance.

We use literature values of river plume properties to calculate $L_{NF}$ for the Fraser (MacDonald & Geyer, 2004), Columbia (McCabe et al., 2008), and Merrimack (MacDonald & Chen, 2012) Rivers. Surf zone widths are approximated using Google Earth as the maximum distance waves break offshore in all available historical images. The channel length for these rivers is taken as the length of the jetty, as measured in a Google Earth image. All three large rivers are in Quadrant (i), indicating that both bathymetric and river dominant conditions lead to freshwater escapes. This is consistent with the engineering present at these river mouths, as well as their large discharges and river mouth velocities.

The range of values for the Quinault is closer to the transition for each axis, but most data are in Quadrants (i), (ii), and (iii), which is consistent with the conceptual model results for the Quinault (section 1.4). The modeling results of Rodriguez et al. (2018) are included (assuming $w_e \approx 10$ mm/s) for four different cases ($Q = 20$ and 100 m$^3$/s, $H_S = 0.6$ and 1 m) and lie in Quadrants (iii) and (iv), indicating that for the parameter space explored in Rodriguez et al. (2018), the wave and river dominant modes are relevant. This is consistent with the scaling developed in Rodriguez et al. (2018), which predicts the escape of river water when river momentum flux is larger than wave momentum flux. This parameter space may thus be helpful to future studies in determining the fate of river water in relation to surf zone wave breaking.

### 4.4. Wave-Current Interaction

The surf zone width calculations (Figure 6b) developed in section 2.3.1 do not include the effects of wave-current interaction, which has a different impact at different wavelengths. In general, an opposing current causes waves to shorten and steepen, as their wavenumber $k$ changes to conserve absolute frequency $\omega = \sqrt{gk \tanh kd} + u \cdot k$, where $u$ is the speed of the current (Mei, 1989). For short waves, this steepening can lead to breaking as the Miche breaking criteria is exceeded (Miche, 1944; Zippel & Thomson, 2017). Short waves also refract to be normal to an opposing current and so a reasonable expectation would be that short waves would refract to be normal to the Quinault outflow before breaking as they oversteepen, while very long (i.e., infragravity) waves could propagate into the estuary (Mei, 1989; Williams & Stacey, 2016). However, some longer waves may simultaneously refract away from the deep channel extending from the river mouth.

The dominance of depth-limited breaking complicates this picture. In order to understand the effects of wave-current interaction at the Quinault, let us first consider the case in which breaking is initiated far offshore of the region of high flow near the channel during low water and/or a period of high waves ($L_{SZ} > L_C$). A wave that has already broken when it encounters the high flow region in the channel will continue to break as the channel deepens nearshore due to the opposing current, causing the surf zone to extend further onshore than shown in Figure 4. In the bathymetric dominance case where depth-limited breaking is initiated onshore of the region of high flow ($L_{SZ} < L_C$), we might expect the currents to play a larger role in the initiation of breaking. What is unclear, however, is where this breaking would occur. In the bathymetric dominance behavior, river water can escape minimally opposed onto the inner shelf, with currents in the range of 0.5–0.75 m/s persisting onto the inner shelf as drifters escape (Figure 3f). Thus, shorter waves may refract toward and break against a current well offshore of $L_{SZ}$ in this case. It is unclear whether such wave breaking would have an impact on the fate of river water, but based on section 4.1, the position of the current-induced wave breaking relative to $L_{NF}$ would likely be important.

## 5. Summary

We present results from an observational study of the Quinault River, a small river that flows into the surf zone in western Washington state. We find that the interaction of the outflow and the surf zone can be characterized in terms of the plume near-field length, $L_{NF}$, the surf zone width, $L_{SZ}$, and the offshore end of the channel, $L_C$, such that three behaviors dominate:

1. River water is trapped within the surf zone and remains fresh when $L_{SZ} > L_{NF}$ & $L_{SZ} > L_C$;
2. River water escapes the surf zone when $L_{NF} > L_{SZ}$ and mixes intensely;
3. River water escapes the surf zone when $L_C > L_{SZ}$ and mixes intensely.

We observe surf zone trapping to be the dominant behavior at the Quinault River, as only one third of drifters escape or nearly escape the surf zone, and river water is rarely observed offshore of the surf zone by nearshore moorings. Maximum drifter excursions are correlated with $L_{NF}$, but the predicted entrainment velocity for the Quinault River plume overestimates the drifter excursions, indicating that wave-induced turbulence may increase plume mixing. Trapped river water propagates a distance into the surf zone roughly equal to $L_{NF}$, at which point its fate is governed by surf zone processes. Extrapolating over the course of 1 year, we find that 70% of river discharge is trapped in the surf zone due to wave dominance.

**Acknowledgments**
This work would not have been possible without the hospitality and local knowledge of the Quinault Division of Natural Resources, particularly Joe Shumacker, Larry Gilbertson, Kristen Phillips, and Kokomo Snell. NSF Grant OCE-1459051 provided funding for this project. Melissa Moulton, Alex De Klerk, and Joe Talbert provided significant assistance with the UAS and buoys. Joel Corlew, Raul Flores, Andy Reay-Ellers, Avery Snyder, and Seth Zippel from the University of Washington Environmental Fluid Mechanics group and Applied Physics Laboratory also assisted with fieldwork. Sarah Giddings, Nirnimesh Kumar, Parker MacCready, and Melissa Moulton provided valuable feedback. Data are available from the Data tab on the SWIFT website (www.apl.uw.edu/SWIFT).

## References

Akan, Ç., Moghimi, S., Özkan-Haller, H. T., Osborne, J., & Kurapov, A. (2017). On the dynamics of the mouth of columbia river: Results from a three-dimensional fully coupled wave-current interaction model. *Journal of Geophysical Research: Oceans*, *122*, 2373–2388. https://doi.org/10.1002/2016JC012307

Brown, J. A., MacMahan, J. H., Reniers, A. J. H. M., & Thornton, E. B. (2015). Field observations of surf zone inner shelf exchange on a rip-channeled beach. *Journal of Physical Oceanography*, *45*(9), 2339–2355. https://doi.org/10.1175/JPO-D-14-0118.1

Christodoulou, G. C. (1986). Interfacial mixing in stratified flows. *Journal of Hydraulic Research*, *24*(2), 77–92.

Clark, D. B., Feddersen, F., & Guza, R. T. (2010). Cross-shore surf zone tracer dispersion in an alongshore current. *Journal of Geophysical Research*, *115*, C10035. https://doi.org/10.1029/2009JC005683

Codiga, D. (2011). Unified tidal analysis and prediction using the UTide Matlab functions [Computer software manual].

Ellison, T. H., & Turner, J. S. (1959). Turbulent entrainment in stratified flows. *Journal of Fluid Mechanics*, *6*, 423–448.

Feddersen, F. (2012). Scaling surf zone turbulence. *Geophysical Research Letters*, *39*, L18613. https://doi.org/10.1029/2012GL052970

Feddersen, F., Guza, R. T., Elgar, S., & Herbers, T. H. C. (1998). Alongshore momentum balances in the nearshore. *Journal of Geophysical Research*, *103*(C8), 15,667–15,676. https://doi.org/10.1029/98JC01270

Feddersen, F., & Trowbridge, J. H. (2005). The effect of wave breaking on surf-zone turbulence and alongshore currents: A modeling study. *Journal of Physical Oceanography*, *35*(11), 2187–2203. https://doi.org/10.1175/JPO2800.1

Fewings, M., Lentz, S. J., & Fredericks, J. (2008). Observations of cross-shelf flow driven by cross-shelf winds on the inner continental shelf. *Journal of Physical Oceanography*, *38*(11), 2358–2378.

Fischer, H. B. E., List, J., Koh, R. C. Y., Imberger, J., & Brooks, N. H. (1979). *Mixing in inland and coastal waters*. San Diego: Academic Press.

Garvine, R. W. (1977). Observations of the motion field of the connecticut river plume. *Journal of Geophysical Research*, *82*(3), 441–454. https://doi.org/10.1029/JC082i003p00441

Garvine, R. W., & Monk, J. D. (1974). Frontal structure of a river plume. *Journal of Geophysical Research*, *79*(15), 2251–2259. https://doi.org/10.1029/JC079i015p02251

Gerbi, G. P., Chant, R. J., & Wilkin, J. L. (2013). Breaking surface wave effects on river plume dynamics during upwelling-favorable winds. *Journal of Physical Oceanography*, *43*, 1959–1980.

Gerbi, G. P., Kastner, S. E., & Brett, G. (2015). The role of whitecapping in thickening the ocean surface boundary layer. *Journal of Physical Oceanography*, *45*(8), 2006–2024.

Haller, M. C., Dalrymple, R. A., & Svendsen, I. A. (2002). Experimental study of nearshore dynamics on a barred beach with rip channels. *Journal of Geophysical Research*, *107*(C6), 14–1–14–21. https://doi.org/10.1029/2001JC000955

Hally-Rosendahl, K., & Feddersen, F. (2016). Modeling surf zone to inner-shelf tracer exchange. *Journal of Geophysical Research: Oceans*, *121*, 4007–4025. https://doi.org/10.1002/2015JC011530

Hally-Rosendahl, K., Feddersen, F., & Guza, R. T. (2014). Cross-shore tracer exchange between the surf zone and inner-shelf. *Journal of Geophysical Research: Oceans*, *119*, 4367–4388. https://doi.org/10.1002/2013JC009722

Hetland, R. D. (2010). The effects of mixing and spreading on density in near-field river plumes. *Dynamics of Atmospheres and Oceans*, *49*, 37–53. https://doi.org/10.1016/j.dynatmoce.2008.11.003

Holman, R. A., Brodie, K. L., & Spore, N. J. (2017). Surf zone characterization using a small quadcopter: Technical issues and procedures. *IEEE Transactions on Geoscience and Remote Sensing*, *55*(4), 2017–2027. https://doi.org/10.1109/TGRS.2016.2635120

Horner-Devine, A. R., Hetland, R. D., & MacDonald, D. G. (2015). Transport and mixing in coastal river plumes. *Annual Review of Fluid Mechanics*, *47*, 569–594.

Izett, J. G., & Fennel, K. (2018). Estimating the cross-shelf export of riverine materials: Part 2. Estimates of global freshwater and nutrient export. *Global Biogeochemical Cycles*, *32*, 176–186. https://doi.org/10.1002/2017GB005668

Janssen, T. T., & Battjes, J. A. (2007). A note on wave energy dissipation over steep beaches. *Coastal Engineering*, *54*(9), 711–716. https://doi.org/10.1016/j.coastaleng.2007.05.006

Jirka, G. H., Adams, E. E., & Stolzenbach, K. D. (1981). Buoyant surface jets. *Journal of the Hydraulics Division, Proc. ASCE*, *107*(HY11), 1467–1487.

Jones, G. R., Nash, J. D., Doneker, R. L., & Jirka, G. H. (2007). Buoyant surface discharges into water bodies. I: Flow classification and prediction methodology. *Journal of Hydraulic Engineering*, *133*(9), 1010–1020.

Jurisa, J. T., Nash, J. D., Moum, J. M., & Kilcher, L. F. (2016). Controls on turbulent mixing in a strongly stratified and sheared tidal river plume. *Journal of Physical Oceanography*, *46*(8), 2373–2388.

Kastner, S. E., Horner-Devine, A. R., & Thomson, J. (2018). The influence of wind and waves on spreading and mixing in the Fraser River plume. *Journal of Geophysical Research: Oceans*, *123*, 6818–6840. https://doi.org/10.1029/2018JC013765

Kilcher, L., Nash, J. D., & Moum, J. N. (2012). The role of turbulence stress divergence in decelerating a river plume. *Journal of Geophysical Research*, *117*, C05032. https://doi.org/10.1029/2011JC007398

Kirby, J. T., & Chen, T.-M. (1989). Surface waves on vertically sheared flows: Approximate dispersion relations. *Journal of Geophysical Research*, *94*(C1), 1013–1027. https://doi.org/10.1029/JC094iC01p01013

Kumar, N., & Feddersen, F. (2017). The effect of stokes drift and transient rip currents on the inner shelf. Part I: No stratification. *Journal of Physical Oceanography*, *47*(1), 227–241. https://doi.org/10.1175/JPO-D-16-0076.1

Longuet-Higgins, M. S. (1970). Longshore currents generated by obliquely incident sea waves: 1. *Journal of Geophysical Research*, *75*(33), 6778–6789.

Longuet-Higgins, M., & Stewart, R. (1961). The changes in amplitude of short gravity waves on steady non-uniform currents. *Journal of Fluid Mechanics*, *10*(4), 529–543.

Longuet-Higgins, M., & Stewart, R. (1962). Radiation stress and mass transport in gravity waves, with application to surf beats. *Journal of Fluid Mechanics*, *13*(4), 481–504.

Luketina, D., & Imberger, J. (1987). Characteristics of a surface buoyant jet. *Journal of Geophysical Research*, *92*(C5), 5435–5447.

MacDonald, D. G., Carlson, J., & Goodman, L. (2013). On the heterogeneity of stratified-shear turbulence: Observations from a near-field river plume. *Journal of Geophysical Research: Oceans*, *118*, 6223–6237. https://doi.org/10.1002/2013JC008891

MacDonald, D. G., & Chen, F. (2012). Enhancement of turbulence through lateral spreading in a stratified-shear flow: Development and assessment of a conceptual model. *Journal of Geophysical Research*, *117*, C05025. https://doi.org/10.1029/2011JC007484

MacDonald, D. G., & Geyer, W. R. (2004). Turbulent energy production and entrainment at a highly stratified estuarine front. *Journal of Geophysical Research*, *109*, C05004. https://doi.org/10.1029/2003JC002094

MacMahan, J. H., Reniers, AdJ. H. M., Thornton, E. B., & Stanton, T. P. (2004). Surf zone eddies coupled with rip current morphology. *Journal of Geophysical Research*, *109*, C07004. https://doi.org/10.1029/2003JC002083

McCabe, R., Hickey, B. M., & MacCready, P. (2008). Observational estimates of entrainment and vertical salt flux in the interior of a spreading river plume. *Journal of Geophysical Research*, *113*, C08027. https://doi.org/10.1029/2007JC004361

Mei, C. C. (1989). *The applied dynamics of ocean surface waves* (Vol. 1). Singapore: World Scientific.

Miche, A (1944). Mouvements ondulatoires de la mer en profondeur croissante ou decroissante. Premiere partie. Mouvements ondulatoires periodiques et cylindriques en profondeur constante. *Annales des Ponts et Chaussees*, *114*, 42–78.

Milliman, J. D., & Syvitski, J. P. M. (1992). Geomorphic/tectonic control of sediment discharge to the ocean: The importance of small mountainous rivers. *The Journal of Geology*, *100*(5), 525–544. https://doi.org/10.1086/629606

O'Donnell, J. (1990). The formation and fate of a river plume: A numerical model. *Journal of Physical Oceanography*, *20*(4), 551–569.

Olabarrieta, M., Geyer, W. R., & Kumar, N. (2014). The role of morphology and wave-current interaction at tidal inlets: An idealized modeling analysis. *Journal of Geophysical Research: Oceans*, *119*, 8818–8837. https://doi.org/10.1002/2014JC010191

Raubenheimer, B., Guza, R. T., & Elgar, S. (1996). Wave transformation across the inner surf zone. *Journal of Geophysical Research*, *101*(C11), 25,589–25,597. https://doi.org/10.1029/96JC02433

Reniers, A. J. H. M., MacMahan, J. H., Thornton, E. B., Stanton, T. P., Henriquez, M., Brown, J. W., et al. (2009). Surf zone surface retention on a rip-channeled beach. *Journal of Geophysical Research*, *114*, C10010. https://doi.org/10.1029/2008JC005153

Rodriguez, A. R., Giddings, S. N., & Kumar, N. (2018). Impacts of nearshore wave-current interaction on transport and mixing of small-scale buoyant plumes. *Geophysical Research Letters*, *45*, 8379–8389. https://doi.org/10.1029/2018GL078328

Stokes, G. G. (1847). On the theory of oscillatory waves. *Transactions of the Cambridge Philosophical Society*, *8*, 441–482.

Thomson, J. (2012). Wave breaking dissipation observed with SWIFT drifters. *Journal of Atmospheric and Oceanic Technology*, *29*(12), 1866–1882. https://doi.org/10.1175/JTECH-D-12-00018.1

Thomson, J., Horner-Devine, A. R., Zippel, S., Rusch, C., & Geyer, W. (2014). Wave breaking turbulence at the offshore front of the Columbia River plume. *Geophysical Research Letters*, *41*, 8987–8993. https://doi.org/10.1002/2014GL062274

Thomson, J., Moulton, M., de Klerk, A., Talbert, J., Guerra, M., Kastner, S. E., et al. (2019). A new version of the swift platform for waves, currents, and turbulence in the ocean surface layer. *Twelfth Current, Waves, and Turbulence Measurement and Applications Workshop*.

Thornton, E. B., & Guza, R. T. (1986). Surf zone longshore currents and random waves: Field data and models. *Journal of Physical Oceanography*, *16*(7), 1165–1178.

Williams, M. E., & Stacey, M. T. (2016). Tidally discontinuous ocean forcing in bar-built estuaries: The interaction of tides, infragravity motions, and frictional control. *Journal of Geophysical Research: Oceans*, *121*, 571–585. https://doi.org/10.1002/2015JC011166

Wong, S. H. C., Monismith, S. G., & Boehm, A. B. (2013). Simple estimate of entrainment rate of pollutants from a coastal discharge into the surf zone. *Environmental Science & Technology*, *47*(20), 11,554–11,561. https://doi.org/10.1021/es402492f

Yuan, Y., & Horner-Devine, A. R. (2013). Laboratory investigation of the impact of lateral spreading on buoyancy flux in a river plume. *Journal of Physical Oceanography*, *43*(12), 2588–2610.

Zippel, S., & Thomson, J. (2015). Wave breaking and turbulence at a tidal inlet. *Journal of Geophysical Research: Oceans*, *120*, 1016–1031. https://doi.org/10.1002/2014JC010025

Zippel, S., & Thomson, J. (2017). Surface wave breaking over sheared currents: Observations from the mouth of the Columbia River. *Journal of Geophysical Research: Oceans*, *22*, 3311–3328. https://doi.org/10.1002/2016JC012498